

Proceedings of the Institution of Mechanical Engineers, Part H: Journal of Engineering in Medicine

<http://pih.sagepub.com/>

Prediction of risk of fracture in the tibia due to altered bone mineral density distribution resulting from disuse: A finite element study

Magnus K. Gislason, Sylvie Coupaud, Keisuke Sasagawa, Yuji Tanabe, Mariel Purcell, David B. Allan and K. Elizabeth Tanner

Proceedings of the Institution of Mechanical Engineers, Part H: Journal of Engineering in Medicine published online 6 February 2014

DOI: 10.1177/0954411914522438

The online version of this article can be found at:
<http://pih.sagepub.com/content/early/2014/02/06/0954411914522438>

Published by:



<http://www.sagepublications.com>

On behalf of:



[Institution of Mechanical Engineers](#)

Additional services and information for *Proceedings of the Institution of Mechanical Engineers, Part H: Journal of Engineering in Medicine* can be found at:

Email Alerts: <http://pih.sagepub.com/cgi/alerts>

Subscriptions: <http://pih.sagepub.com/subscriptions>

Reprints: <http://www.sagepub.com/journalsReprints.nav>

Permissions: <http://www.sagepub.com/journalsPermissions.nav>

>> [OnlineFirst Version of Record - Feb 6, 2014](#)

[What is This?](#)

Prediction of risk of fracture in the tibia due to altered bone mineral density distribution resulting from disuse: A finite element study

Magnus K. Gislason^{1,2}, Sylvie Coupaud^{1,3}, Keisuke Sasagawa^{4,5},
 Yuji Tanabe⁵, Mariel Purcell³,
 David B. Allan³ and K. Elizabeth Tanner⁴

Abstract

The disuse-related bone loss that results from immobilisation following injury shares characteristics with osteoporosis in post-menopausal women and the aged, with decreases in bone mineral density leading to weakening of the bone and increased risk of fracture. The aim of this study was to use the finite element method to: (i) calculate the mechanical response of the tibia under mechanical load and (ii) estimate of the risk of fracture; comparing between two groups, an able-bodied group and spinal cord injury patients group suffering from varying degrees of bone loss. The tibiae of eight male subjects with chronic spinal cord injury and those of four able-bodied age-matched controls were scanned using multi-slice peripheral quantitative computed tomography. Images were used to develop full three-dimensional models of the tibiae in Mimics (Materialise) and exported into Abaqus (Simulia) for calculation of stress distribution and fracture risk in response to specified loading conditions – compression, bending and torsion. The percentage of elements that exceeded a calculated value of the ultimate stress provided an estimate of the risk of fracture for each subject, which differed between spinal cord injury subjects and their controls. The differences in bone mineral density distribution along the tibia in different subjects resulted in different regions of the bone being at high risk of fracture under set loading conditions, illustrating the benefit of creating individual material distribution models. A predictive tool can be developed based on these models, to enable clinicians to estimate the amount of loading that can be safely allowed onto the skeletal frame of individual patients who suffer from extensive musculoskeletal degeneration (including spinal cord injury, multiple sclerosis and the ageing population). The ultimate aim is to reduce fracture occurrence in these vulnerable groups.

Keywords

Spinal cord injury, disuse osteoporosis, fracture risk, paraplegia, finite element model

Date received: 13 September 2013; accepted: 3 January 2014

Introduction

As Wolff described as early as 1892, bone adapts to its loading history. A possible mechanism was proposed by Frost in his Mechanostat Theory. He conceptualised a control system for triggering adaptation within bone, based on strain thresholds.¹ This theory states that at high physiological loading net bone formation occurs in response to high strains (overuse), while net bone resorption occurs when strains are unusually low (disuse). Additional factors such as strain rate² and other theories of adaptation such as cellular accommodation^{3,4} provide alternative explanations of bone remodelling.

An example of bone's adaptation to disuse occurs after spinal cord injury (SCI). In people with paraplegia

¹Departments of Mechanical and Biomedical Engineering, University of Strathclyde, Glasgow, UK

²Department of Biomedical Engineering, School of Engineering and Technology, University of Reykjavik, Reykjavik, Iceland

³Scottish Centre for Innovation in Spinal Cord Injury, Queen Elizabeth National Spinal Injuries Unit, Southern General Hospital, Glasgow, UK

⁴Department of Biomedical Engineering, University of Glasgow, Glasgow, UK

⁵Department of Mechanical and Production Engineering, Niigata University, Niigata, Japan

Corresponding author:

M Gislason, Department of Biomedical Engineering, School of Engineering and Technology, University of Reykjavik, Menntavegi 1, 101 Reykjavik, Iceland.

Email: magnuskg@ru.is

or quadriplegia who are dependent on wheelchairs for their mobility, previously weight-bearing parts of the skeleton are no longer required to be the major structural support of the body. Prior to injury dynamic loading also results from muscle action on the long bones (tibia, fibula, femur). This is lost after SCI. SCI is an extreme example of disuse, but similar manifestations of disuse adaptation of bone are found in multiple sclerosis, stroke, ageing, long-term bed rest and in astronauts exposed to weightlessness for a prolonged period of time.^{5–9}

Risk of fracture (RF) in SCI patients increases with disuse-related bone loss despite relative immobility post-injury. Lower-limb fractures are at least twice as common in SCI patients than in the general population, with the RF increasing with time since injury.¹⁰ Vestergaard et al.¹¹ reported that fractures occur in 2%–6% of people who have suffered a SCI. Cross-sectional densitometry studies^{12,13} describe an exponential decrease in bone mineral density (BMD) in the first 3 years after SCI, with BMD reaching a steady-state condition at around 3–7 years post-injury, after which time chronic SCI patients are most susceptible to fracture.¹⁴ A disuse-adapted bone contains less bone material and therefore is structurally weaker than a healthy bone of similar length. This reduction makes the disuse-adapted bone more likely to break, leading to so-called ‘fragility fractures’ or ‘osteoporotic fractures’. Fractures resulting from disuse osteoporosis after SCI are typically sustained as a result of a fall from a wheelchair or while the person transfers between two surfaces (e.g. between wheelchair and bed) and over 80% occur in the long bones.¹⁵ Evidence suggests that tibial fractures account for 18% of all fractures after SCI,¹⁶ and other more recent studies suggest that 84% of all fractures occur in the legs, with 62% occurred below the knee in the tibia and fibula, compared to 38% above the knee.¹⁷

BMD status from detailed bone scans can indicate to clinicians an individual patient’s fracture susceptibility and provide the opportunity for targeted, patient-specific intervention aimed at reducing fractures in the most vulnerable patients. Three-dimensional (3D) computer-generated models of bones that incorporate BMD distribution information along the whole bone may give an indication of fracture susceptibility, help to identify probable fracture sites and ultimately be used to target interventions to the weakest areas. This could lead to stratified therapy according to the level of RF, prioritising the patients in greatest need of treatment, and targeting the weakest regions of the bone for treatment. For this patient-specific approach to be valid, the computer-generated models of the bones must be based on *in vivo* data from the individual, and the imaging resolution needs to be sufficient to map BMD throughout the bone.

Peripheral quantitative computed tomography (pQCT) allows discrimination between trabecular (cancellous or spongy) and cortical (compact) bone to obtain true volumetric BMD measurements of each compartment and to determine the geometrical

properties of the bone. pQCT has been validated for quantifying BMD reduction in SCI patients^{12,13} and has recently been shown to have predictive capacity in the early stages of bone loss, based on repeat scans carried out within the first few months of SCI.¹⁸ This study showed that pQCT can identify those patients with the most severe disuse-related bone loss, similar to the pQCT-based stratification into slow- or fast-progressing bone loss suggested previously for women with post-menopausal osteoporosis.¹⁹ Trabecular BMD measured using pQCT has been shown to be the parameter that best discriminates between individuals who do or do not sustain fractures after SCI.¹⁴ As BMD provides a surrogate measure of fracture risk, detailed measurements of altered BMD distribution in a bone that has adapted (or is in the process of adapting) to disuse could be used to make patient-specific predictions of susceptibility to fragility fracture. To achieve this, quantitative information from pQCT scans can be fed into 3D computational bone models and finite element (FE) methods used to carry out detailed analyses of the bone structure and to simulate fracture scenarios.

Computational methods, such as the FE method, to estimate bone stresses are well established in relation to osteoporosis and osteoarthritis. Various studies have investigated the microscopic properties of osteoarthritic bone using high-resolution (HR) pQCT imaging to capture trabecular structure.²⁰ During the scanning process, the image voxel-edge size is often close to 100 µm, and the FE models are created by converting each voxel into a brick element. Due to its HR, this method gives an accurate representation of the trabecular structure and its response under loading. Using this technique, Boutroy et al.²⁰ reported a failure load of 2.48 kN in the radius for osteoporotic patients, compared to 2.93 kN for able-bodied (AB) controls. Other studies have reported failure loads of 3.47²¹ and 3.8 kN²² for AB subjects in the radius. Using FE analysis, Vilayaphiou et al.²³ reported a failure load of 6.64 kN in the tibia in osteoporotic post-menopausal women compared to 7.55 kN in AB controls. The use of such micro-FE models is difficult when modelling large areas of the bone due to scanning limitations and computational restrictions, as the number of elements required would be tens or hundreds of millions.

There are only a few studies that focus on the macroscopic behaviour of osteoporotic bone to identify the critical load and possible fracture sites. In this article, FE models are presented, based on actual BMD distribution for use in simulating the stress-strain patterns in the bone under different loading conditions. The hypothesis is that FE models based on BMD distribution measured *in vivo* from multi-slice pQCT scans taken along the length of the tibia can be used to identify regions most susceptible to fracture in people with low BMD. The results obtained from such models could give clinicians important information to allow treatment to slow down the effects of osteoporosis to be planned, by stratifying patients according to their individual

Table 1. Characteristics for able-bodied (AB) and spinal cord injured (SCI) subjects.

Subject	Age	Time since injury
AB1	34	—
AB2	27	—
AB3	42	—
AB4	20	—
SCI1	31	3
SCI2	28	1.5
SCI3	46	1.5
SCI4	17	4
SCI5	42	23
SCI6	24	2
SCI7	47	27
SCI8	43	20

Age of each subject and time since injury for cases of SCI are given in years.

predicted RF and targeting treatment to those at highest risk.

Methods

Men (16 + years old) with established motor-complete SCI at neurological level C4 or below were identified through the Queen Elizabeth National Spinal Injuries Unit in Glasgow. In parallel, age-matched AB male controls were recruited. Ethical approval for the study was granted by the National Health Service Greater Glasgow & Clyde West of Scotland Research Ethics Committee 5 (Ref: 11/AL/0043). Each subject provided informed consent prior to participation in the study, in line with the Declaration of Helsinki.

Eight male subjects from the SCI group and four male subjects from the AB group were recruited for the study. For the SCI group, time since injury (mean \pm standard deviation (SD)) was 10.3 ± 11.0 years and age was 34.8 ± 11.3 years old; for the AB control group, age was 30.8 ± 9.4 years old (Table 1). The age-matched groups were considered as AB1 being the control for SCI1, AB2 for SCI2 and SCI6, AB3 for SCI3, SCI7 and SCI8, while AB4 was the control for SCI4. Tibia lengths were 394.4 ± 19.2 mm and 400.0 ± 12.3 mm in the SCI and AB groups, respectively. The number of pQCT image slices taken along the length of the bone ranged from 24 (for SCI1) to 43 slices (for AB1), with a mean \pm SD of 34.7 ± 4.3 . For SC1, the scanning session was terminated before the full set of images could be taken, as severe lower-limb spasticity led to excessive movement artefact. Total effective radiation dose for each subject was less than $30 \mu\text{Sv}$.

The length of the tibia was measured for each subject from the medial malleolus to the medial joint cleft of the knee. A pQCT scanner (XCT3000, Stratec Medizintechnik GmbH, Germany) was used for in vivo imaging, to scan the tibia in two sections (distal then proximal). Images were 2 mm thick, with an in-plane resolution of $0.5 \text{ mm} \times 0.5 \text{ mm}$. Images were taken at intervals of 1% of total tibia length in the epiphyses (7

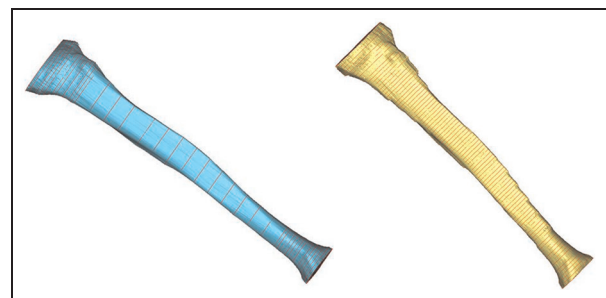


Figure 1. Location of original (real) image slices taken using pQCT (left) along the length of the tibia of an able-bodied subject (AB1) and the locations of re-sampled (interpolated) image slices used for the 3D model (right). Each slice location is shown as a line across the bone.

slices distally, 10 slices proximally) and at 4%–5% intervals of the tibial length in the diaphysis. The manufacturer's software (XCT5.50, Stratec Medizintechnik GmbH, Germany) was used to export images as comma separated voxel (CSV) files, composed of matrices of BMD values for each individual voxel of the cross-sectional images. The CSV files were converted to bitmap images in MATLAB (MathWorks) before being imported into Mimics (Materialise, Leuven, Belgium) where the segmentation of each tibia was performed and a 3D model created. To compensate for large slice intervals in the diaphyseal section of the tibia, resampling by interpolation between slices was performed to smooth the surface model and volume mesh. For this, a cubic interpolation algorithm was used, resulting in a regular slice thickness of 1% of total bone length (see Figure 1).

The tibiae were meshed with surface triangular elements. The quality of the mesh was determined from the equi-angle skewness ratio, which was defined using equation (1)

$$\min\left(\frac{\alpha}{60} : \frac{180 - \beta}{180 - 60}\right) \quad (1)$$

where α was the smallest angle of the triangle and β the largest. Ideally, the ratio should be unity, corresponding to an equilateral triangle. Surface element checks revealed that the lowest equi-angle skewness (mean \pm SD) was 0.53 ± 0.06 and the percentage of element exceeding the ratio 0.9 were on average $92\% \pm 5\%$, thus confirming the quality of the mesh.

Each subject's tibia surface mesh was imported into Abaqus (v.6.10, Simulia) for conversion into a volumetric mesh, using 4-node tetrahedral elements (C3D4). Quality checks were performed on the volumetric mesh and the results showed that the average aspect ratio was 1.57 ± 0.01 and the worst aspect ratio was on average 3.62 ± 0.24 , so that all the tetrahedral elements were well shaped. Experiments were carried out with quadratic elements and it was seen that changing the 4-node elements to 10-node tetrahedral elements did not alter the stress profile, so 4-node tetrahedral elements were used to minimise computing time. The mean and

standard deviation of the number of elements for each model was 775600 ± 95383 resulting in an average element density of 2.9 elements/mm³. The volumetric mesh was re-imported into Mimics, where the material assignment of each element was carried out, with a constant Poisson's ratio of 0.3. The maximum BMD for each subject was obtained from the pQCT scans and used to normalise the greyscale values of the images and convert to BMD, using a linear relationship between greyscale values and BMD. Young's modulus was calculated from BMD using a power law from Keller,²⁴ equation (2)

$$E(\rho) = 10500 * \rho_{BMD}^{2.29} \quad (2)$$

where the BMD ρ_{BMD} is in gram per cubic centimetre and Young's modulus, E , in megapascal. The ultimate strength of the bone was estimated using empirical expressions relating the density to the ultimate stress from Keyak et al.²⁵ and Keller,²⁴ equation (3)

$$\sigma_{UTS} = \begin{cases} 137 * \rho_{BMD}^{1.88}, & \rho < 0.317 \\ 114 * \rho_{BMD}^{1.72}, & \rho \geq 0.317 \end{cases} \quad (3)$$

where the ultimate strength, σ_{UTS} , is in megapascal.

Simplified loading conditions were applied to the bones. Experimental and computational studies^{26–29} have shown that the in vivo knee joint contact forces in AB subjects are around three times bodyweight and that the tibia is able to withstand compressive forces of 7.5 kN²³ in an AB control group consisting of post-menopausal women. In the presented study, four simplified loading conditions were applied in compression (8000 N), torsion (70 N m) and bending (300 N m antero-posteriorly and latero-medially), for both the SCI and AB models. In compression, the load was distributed 60% onto the medial and 40% onto the lateral condyles, and the distal end of the tibia was fixed in all directions, both rotational and translational (Figure 2(a)). The locations of the loading surfaces corresponded with those of Iwaki et al.³⁰ For bending and torsion, the proximal end of the tibia was fixed in all directions

(Figure 2(b)). The bone was simulated as a cantilever beam where a bending force equivalent to 300 N m was applied at the distal portion in the antero-posterior direction or latero-medial direction, respectively. For torsional loading, the distal tibia was embedded in a rigid cube, with edge length of 70 mm, subjected to 70 N m torque. The loading was the same for all subjects and not corrected to the individual's weight.

Human bones have a complicated structure, and the failure criteria of bone have been discussed extensively.³¹ Bessho et al.³² used the Drucker–Prager strain-level-based yield criteria and determined that once an element had exceeded 10,000 $\mu\epsilon$ (microstrain), it was deemed to have failed. In this study, the RF was calculated for each element, based on the ratio of von Mises stress, σ_{vm} , to the yield stress, σ_{UTS} (according to equations by Keyak et al.²⁵ and Keller²⁴), as described in equation (4)

$$RF = \frac{\sigma_{vm}}{\sigma_{UTS}} \quad (4)$$

A fracture was determined if the ratio RF exceeded 1.

Results

Differences in BMD distribution and bone structure between SCI1 and his AB control can be seen clearly in the original pQCT images shown for selected sites (proximal epiphysis, mid-shaft and distal epiphysis) in Figure 3. SCI1 has much reduced BMD throughout the epiphyseal cross-sections (5% and 95% slice locations) compared to AB1. Differences in cortical bone in the mid-shaft (40% slice location) between AB and SCI subjects are less clear in some cases, and show a high degree of inter-subject variability.

This inter-subject variability after SCI is confirmed by looking in detail in Figure 4 at the percentage of model elements assigned low BMD values (corresponding to trabecular bone) and the percentage of model elements assigned high BMD values (cortical bone) based on pQCT-derived greyscale values. The distribution of

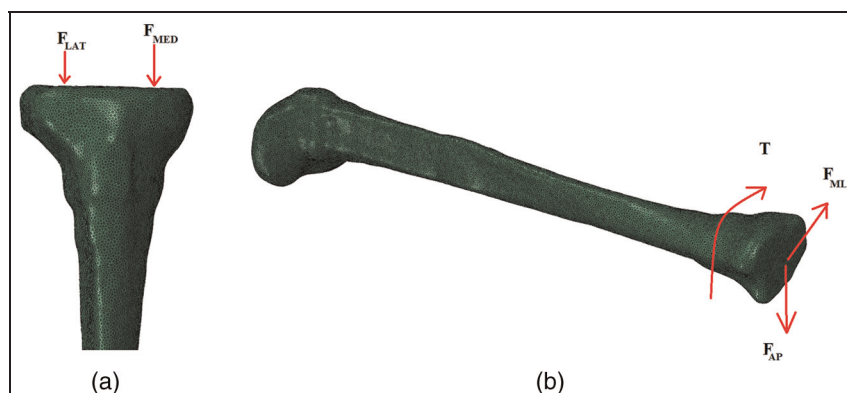


Figure 2. Illustration of loading scenarios used in stress/strain and risk of fracture simulations: (a) in compression with loading distributed on lateral (F_{LAT}) and medial (F_{MED}) condyles (left), (b) torsion by applying torque (T) and bending by applying force at the proximal end, with the distal tibia fixed – AP bending was achieved by applying antero-posterior force (F_{AP}) and ML bending by applying medio-lateral force (F_{ML}).

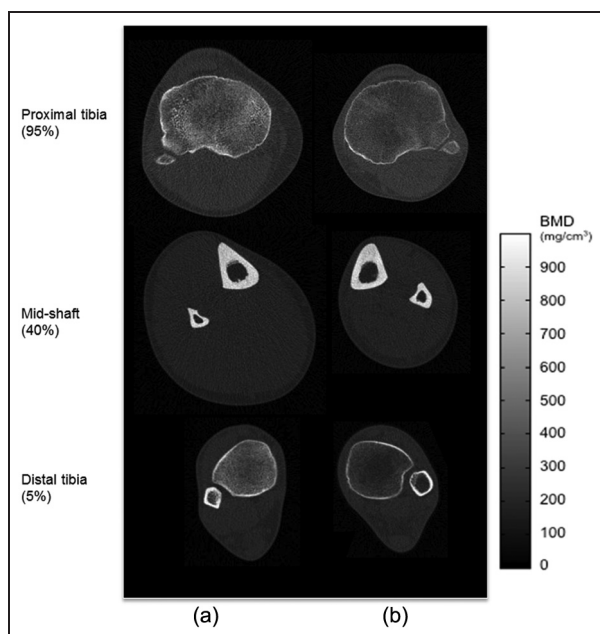


Figure 3. Comparison of pQCT images at proximal tibia (top), 40% mid-shaft tibia (middle) and distal tibia (bottom) for (a) ABI's left lower leg, and (b) SCI1's right lower leg. The scale for bone mineral density values, relating to greyscale values, is given in the legend on the right.

These images are not to the same size scale.

elements along the BMD spectrum is shown for each AB subject individually in Figure 4(a), and for each SCI subject in Figure 4(b). In most subjects, there is a double-peak in the histogram, with one peak representing mostly trabecular bone (at the low BMD end of the spectrum) and another representing cortical bone (at the high BMD end). SCI8 is an exception, showing a much higher percentage of low BMD elements than other subjects, and no clear peak in the percentage of high BMD elements.

The original pQCT images for each subject were taken at relatively large image slice intervals in the diaphysis (see Figure 1). Re-sampling the imaging data was required to create the full 3D volume mesh, and interpolation resulted in a regular slice interval throughout the bone. This allowed FE analysis to be performed on each individualised tibia model (e.g. Figure 5(a)) to simulate the loading on the bone. Figure 5(b) shows the density distribution in the tibia as a function of its normalised length. The effects of the interpolation can be seen from the graph as oscillating values in BMD, which would not be expected physiologically.

The common feature of altered BMD distribution is that all subjects with chronic SCI have lower BMD at the epiphyses than their controls, which is to be expected as these are known fracture-prone sites. Most of the SCI subjects (SCI1–3 and SCI5–7) in this study do not have noticeably weakened tibial shafts, with similar local BMD distribution as their controls. Two exceptions include one young male subject (SCI4) who was the youngest at the time of his injury and who has

lost bone extensively in both the epiphyses (trabecular bone) and diaphysis (cortical bone) with consequently increased RF seen throughout the distal half of the bone and in the proximal epiphysis (Figure 6). The second subject with substantially increased calculated risks of fracture is SCI8, who is one of the three subjects who were scanned more than 20 years post-injury. Both SCI4 and SCI8 have suffered fractures in the contralateral limb in the past.

The altered BMD distribution throughout the bone in SCI4 and SCI8 translates into differences in structural integrity of the tibial shaft in these particular subjects, compared to all other SCI subjects and AB controls, when loading is applied. When the Von Mises stresses are plotted for each of the four loading conditions for all subjects, the highest stresses are seen around the proximal and distal end of the tibial diaphysis. For the bending load, the highest stresses were 134 MPa tensile and 188 MPa compressive. RF was calculated by comparing the stress value in each element to the ultimate stress value for the corresponding element calculated using equations (3) and (4). For each of the loading simulations, compression, antero-posterior (AP) bending, medio-lateral (ML) bending and torsion, the percentage of elements where the RF ratio exceeded 1 is shown in Table 2. Overall, the percentage of elements that would fracture under the loading conditions imposed was greater in SCI subjects than in their age-matched AB controls. The differences were modest in some cases (e.g. SCI3 compared to AB3), but SCI4 and SCI8 are clear outliers, exhibiting failure of approximately 12% of elements under physiological loading in torsion and both AP and ML bending for SCI4 and between 18% and 24% for SCI8, compared to < 1.3% in all other subjects. Considering the four SCI patients in their forties and their control (SCI3, SCI5, SCI7, SCI8 and AB3) there are three long-term injured patients, yet only one of these has substantially increased RF. While these are far too few subjects for statistical analysis, this trend does agree with the clinical observation that some long-term SCI patients suffer minimal effects on their bone mass and limited RF whereas other patients have substantial reductions and a history of low trauma fractures. This observation illustrates the value of patient-specific predictions, achievable using individual pQCT-based FE models.

Discussion

By developing individualised tibia models for SCI patients and AB controls, altered BMD throughout the bone has been shown to affect fracture susceptibility. This paper provides a proof-of-concept that FE models can be used to identify the regions of the tibia most likely to fracture under certain loading scenarios, as well as the relative RF, on a patient-specific basis.

Other models, based on magnetic resonance imaging and/or clinical CT, typically have not included HR

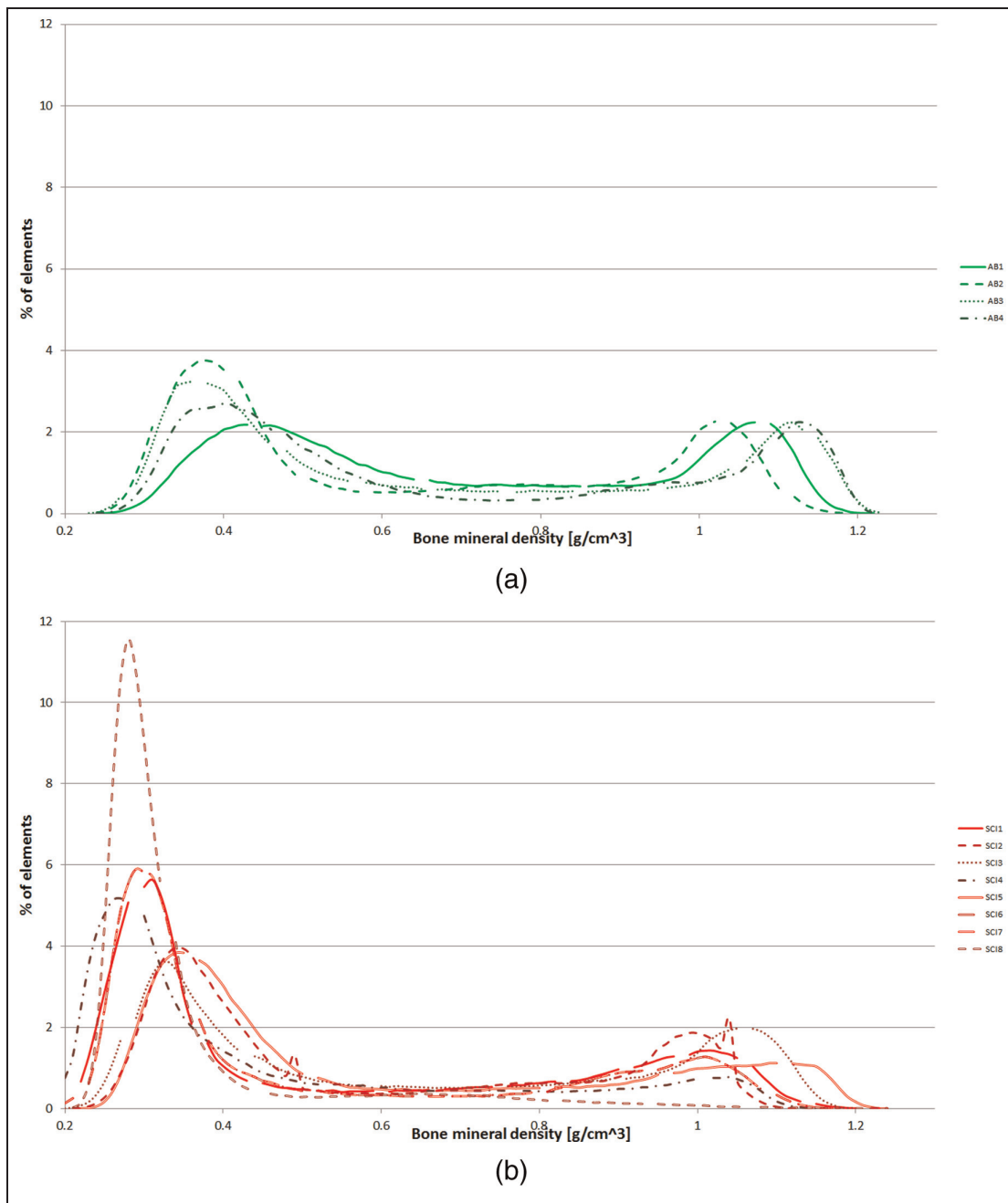


Figure 4. Histograms showing the percentage of elements assigned different bone mineral density (BMD) values in individualised models: (a) for able-bodied subjects (top) and (b) SCI subjects (bottom). The BMD value assigned to each element is based on the pQCT-derived greyscale value.

information on the BMD values in the individual voxels. In the present study, pQCT images were taken through the whole length of the tibia and the FE models created include detailed patient-specific mapping of mechanical properties calculated from the BMD values. The FE technique provides a detailed representation of the bone's geometry and the models constructed combine information about BMD distribution, geometry and thus load distribution, throughout the bone. This information contributes to enhancing the understanding of the bone's mechanical response to loading in individual patients. In the long-term, understanding the response of osteoporotic bone to mechanical loading

should enable prediction of the amount of loading each patient is able to withstand, with the aim of reducing future fractures.

The increased incidence of fractures in the long bones of the paralysed limbs after SCI in certain patients is associated with the reduced bone mineral content and altered BMD distribution throughout the bone. Bone weakness in chronic SCI results from the bone's adaptive response to the substantially reduced mechanical loading, which is typically more pronounced at the epiphyses. These are the typical patterns, but the patient-specific 3D tibia models developed in this study for eight SCI subjects and their

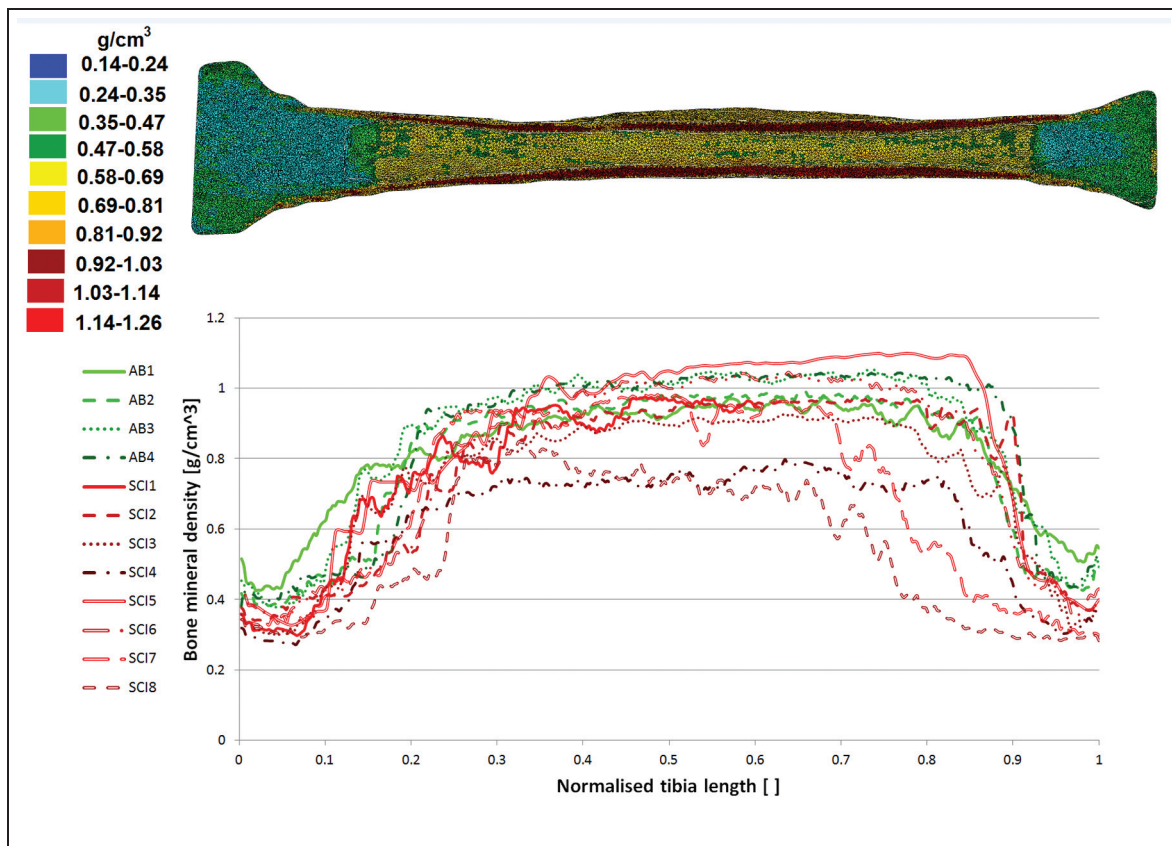


Figure 5. Bone mineral density (BMD) variations in patient-specific models, based on multi-slice pQCT imaging along the length of the tibia: (a) an example of element-by-element distribution of model elements along one subject's tibia (AB3), with BMD values between 0.14 and 1.26 g/cm³; and (b) variation in mean BMD distribution along the length of the tibia shown for each of the subjects (AB 1–4, and SCI1–8), from the proximal end (0) to the distal end (1) of the bone. BMD values between measured slices were calculated by interpolation.

AB: able-bodied; SCI: spinal cord injury.

Table 2. Percentage of elements failing (according to the risk of failure criteria) for each subject's tibia, based on a finite element simulation, with loading applied in compression, bending (AP and ML) and torsion.

Subject	Compression (%)	AP bending (%)	ML bending (%)	Torsion (%)
AB1	< 0.01	0.01	< 0.01	0.02
AB2	0.11	0.04	0.07	< 0.01
AB3	< 0.01	0.15	0.15	< 0.01
AB4	0.58	0.12	2.02	0.76
SCI1	0.06	1.21	3.86	0.55
SCI2	0.01	0.24	0.30	0.01
SCI3	0.21	0.19	0.15	0.00
SCI4	1.91	12.10	11.88	11.80
SCI5	0.01	0.73	1.20	0.28
SCI6	0.58	0.33	0.82	< 0.01
SCI7	1.35	2.83	3.33	0.00
SCI8	18.09	24.11	19.87	21.69
Average AB	0.17	0.08	0.53	0.20
All SCI	2.78	5.22	0.53	4.64
SCI excluding SCI4 and SCI8	0.37	0.92	1.61	0.60

AB: able-bodied; SCI: spinal cord injury; AP: antero-posterior, ML: medio-lateral.

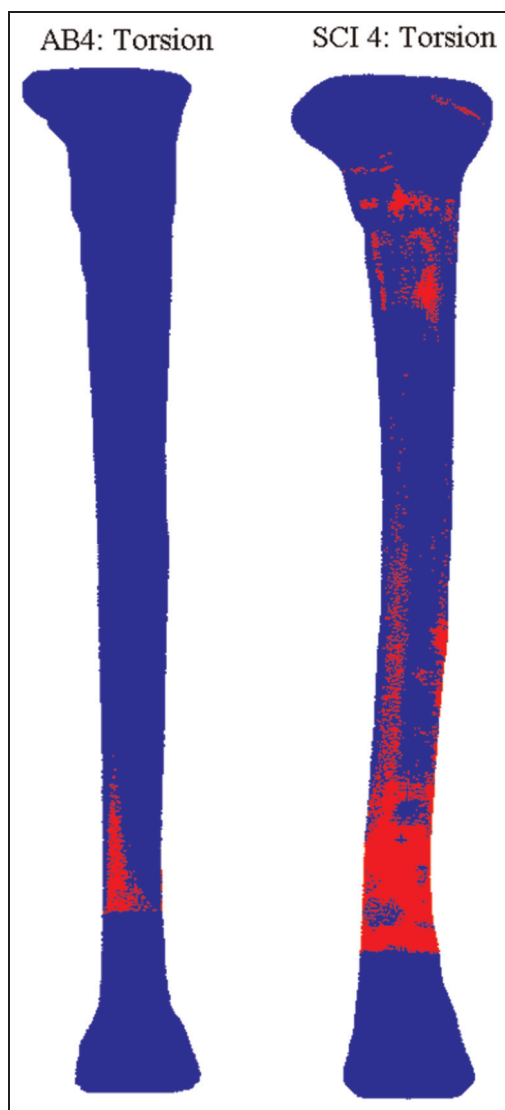


Figure 6. Tibiae loaded in torsion showing areas where the risk of fracture is above 1 for both AB4 and SCI4, an age-matched pair of young subjects.
AB: able-bodied; SCI: spinal cord injury.

four AB age-matched controls show that the pattern of altered BMD distribution after SCI differs substantially between individuals. For example, SCI4 and SCI8 exhibit consistently low BMD throughout their bones (including the shaft), whereas other SCI subjects show decreased BMD at the epiphyses only, with similar BMD distribution in the diaphysis compared to AB controls. To quantify the effects of inter-subject differences, physiological loading was applied to each model to determine the regions of weakness under different loading scenarios (compression, AP and ML bending, torsion). In compression, the 8.0 kN compressive load applied represented 10 times average body weight, while Liu et al.³³ suggest an average failure load for the tibia of 4.688 ± 1.262 kN. SCI patients do not generate such loads, as they spend a considerable amount of time sitting; thus, compression loading is not the greatest cause for concern in SCI. However, it is necessary

to consider such loading to compare the RF relative to AB subjects whose tibiae would be exposed to higher loads during normal weight-bearing activities.

Bending and torsional loading are more clinically relevant, being the probable causes of SCI fractures, such as falling from a wheelchair or transfer between two surfaces. Preliminary simulations of bending and torsion already suggest increased RF for two of these eight SCI subjects under this loading and the RF in bending and torsion provides an indication of which patients should be targeted for osteoporosis treatment. In SCI48, there is minimal increase in the RF under axial loading, but increases in RF are seen in bending and torsion, while SCI4 has increased RF in all loading directions. For SCI subjects, there was inter-subject variation in the response to bending and torsional loading, which may be related to inter-subject differences in the porosity of the trabecular network at the epiphyses. Different degrees of trabecular porosity could have consequences on local structural integrity, but further work is needed to quantify the full extent of the different spatial patterns of bone loss on the RF in different people.

For the osteoporotic tibia, most of the published fracture analysis has been carried out at a microscopic level, identifying the failure mechanics of individual trabeculae within a small region of the bone. This study looks at how the whole bone responds to various types of physically relevant loading conditions which the micro-FE modelling is unable to capture. The major advantage of pQCT over micro-CT is that sections of the whole bone can be scanned in a clinically sensible time, with precise variations in the bone mineral level plotted and used to calculate the local mechanical properties. Furthermore, the radiation dose from pQCT is lower than a full tibial CT scan. Such a macroscopic model can give clinicians important information about which patients are most susceptible to fractures.

Data obtained from SCI patients who experience disuse-related bone loss have shown the clinical potential for 3D computational models. The same principles are applicable to a number of clinical groups. There is a need to understand the macro-structural behaviour of the long bones to optimise treatments for musculoskeletal degeneration after stroke, multiple sclerosis and in relation to the natural declines that occur with ageing.

Limitations

There are limiting factors in this study. Due to the nature of the scans, each slice imaging took 3 min, meaning that the numbers of slices were limited to an average of 35 in order not to cause discomfort to the subject. Interpolation of the images was used to increase the number of slices to obtain the geometrical model of the bone, but could be a source of errors in the material distribution within the bone.

The loading conditions were assumed equal between the two groups. Biomechanical models have been published that predict the in vivo loading conditions on the distal tibia for AB persons but less is known about the in vivo loading conditions to which SCI patients could potentially be subjected. In order to compare the two types of bones, the same loading scenario was assumed between the groups, but in future studies the influence of patient weight could be included. Determining the absolute fracture load using the FE method can be subjected to errors as many fracture criteria are possible as well as elements showing high non-physiological loading due to boundary condition effects or other numerical instabilities. This study only reports on the relative fracture risk between the two groups under a fixed load. The modelling was linear elastic, based on 100 different material models based on the density values. Future work could look into the effects of non-linear material models.

Conclusion

In this study, multi-slice pQCT images from SCI patients with disuse-related bone loss have provided a unique insight into the mechanical behaviour of osteoporotic bone. FE models of the tibia have been developed elsewhere, but the models described here show the potential for patient-specific FE models to stratify patients into risk categories, by tailoring individual fracture risk prediction. Quantification of patient-specific fracture susceptibility, including locating the regions most likely to fracture under simulated physiological loading, is illustrated using the percentage of elements expected to fracture. Such models still require validation, but are promising tools for the development of individualised rehabilitation intervention design. These would enable clinicians to target bone-stimulating interventions to those patients who would benefit most.

Acknowledgements

We are grateful to the patients and other volunteers who took part, NHS Greater Glasgow & Clyde R&D for sponsoring the study and staff at the Queen Elizabeth National Spinal Injuries Unit for help with recruitment and scanning. Thanks also to Dr Caroline Findlay for her file conversion code for pQCT images.

Declaration of conflicting interests

The authors have no conflicts of interest to declare.

Funding

Funding was provided by the Scottish Funding Council's Glasgow Research Partnership in Engineering for Dr Coupaud and Prof Tanner, the Royal Society of Edinburgh's International Exchange Programme for an initial short visit from Dr Sasagawa

to Glasgow and Niigata Engineering Promotion Society's scheme for supporting a subsequent 1-year secondment for Dr Sasagawa to continue his research at the University of Glasgow.

References

1. Frost H. Perspectives: a proposed general model of the 'mechanostat'. *Anat Rec* 1996; 244(2): 139–147.
2. Rubin C, Turner AS, Mallinckrodt C, et al. Mechanical strain, induced noninvasively in the high-frequency domain, is anabolic to cancellous bone, but not cortical bone. *Bone* 2002; 30(3): 445–452.
3. Schriefer JL, Warder SJ, Saxon LK, et al. Cellular accommodation and the response of bone to mechanical loading. *J Biomech* 2005; 38(9): 1838–1845.
4. Turner CH. Toward a mathematical description of bone biology: the principle of cellular accommodation. *Calcif Tissue Int* 1999; 65(6): 466–471.
5. Bloomfield SA. Changes in musculoskeletal structure and function with prolonged bed rest. *Med Sci Sports Exerc* 1997; 29(2): 197–206.
6. De Bruin ED, Vanwanseele B, Dambacher MA, et al. Long-term changes in the tibia and radius bone mineral density following spinal cord injury. *Spinal Cord* 2005; 43(2): 96–101.
7. Ozgocmen S, Bulut S, Ilhan N, et al. Vitamin D deficiency and reduced bone mineral density in multiple sclerosis: effect of ambulatory status and functional capacity. *J Bone Miner Metab* 2005; 23(4): 309–313.
8. Smeltzer SC, Zimmerman V and Capriotti T. Osteoporosis risk and low bone mineral density in women with physical disabilities. *Arch Phys Med Rehabil* 2005; 86(3): 582–586.
9. Vico L, Collet P, Guignandon A, et al. Effects of long-term microgravity exposure on cancellous and cortical weight-bearing bones of cosmonauts. *Lancet* 2000; 355(9215): 1607–1611.
10. Zehnder Y, Markus Lüthi M, Michel D, et al. Long-term changes in bone metabolism, bone mineral density, quantitative ultrasound parameters, and fracture incidence after spinal cord injury: a cross-sectional observational study in 100 paraplegic men. *Osteoporos Int* 2004; 15(1): 180–189.
11. Vestergaard P, Krogh K, Rejnmark L, et al. Fracture rates and risk factors for fractures in patients with spinal cord injury. *Spinal Cord* 1998; 36(11): 790–796.
12. Eser P, Frotzler A, Zehnder Y, et al. Relationship between the duration of paralysis and bone structure: a pQCT study of spinal cord injured individuals. *Bone* 2004; 34(5): 869–880.
13. Coupaud S, McLean AN and Allan DB. Role of peripheral quantitative computed tomography in identifying disuse osteoporosis in paraplegia. *Skeletal Radiol* 2009; 38(10): 989–995.
14. Eser P, Frotzler A, Zehnder Y, et al. Fracture threshold in the femur and tibia of people with spinal cord injury as determined by peripheral quantitative computed tomography. *Arch Phys Med Rehabil* 2005; 86(3): 498–504.
15. Morse LR, Battaglino RA, Stolzman KL, et al. Osteoporotic fractures and hospitalization risk in chronic spinal cord injury. *Osteoporos Int* 2009; 20(3): 385–392.
16. Ragnarsson KT and Sell GH. Lower extremity fractures after spinal cord injury: a retrospective study. *Arch Phys Med Rehabil* 1981; 62(9): 418–423.

17. Lazo MG, Shirazi P, Sam M, et al. Osteoporosis and risk of fracture in men with spinal cord injury. *Spinal Cord* 2001; 39(4): 208–214.
18. Coupaud S, McLean AN, Lloyd S, et al. Predicting patient-specific rates of bone loss at fracture-prone sites after spinal cord injury. *Disabil Rehabil* 2012; 34(26): 2242–2250.
19. Dambacher MA, Neff M, Kissling R, et al. Highly precise peripheral quantitative computed tomography for the evaluation of bone density, loss of bone density and structures. *Drugs Aging* 1998; 12(Suppl. 1): 15–24.
20. Boutroy S, Van Rietbergen B, Sornay-Rendu E, et al. Finite element analysis based on in vivo HR-pQCT images of the distal radius is associated with wrist fracture in postmenopausal women. *J Bone Miner Res* 2008; 23(3): 392–399.
21. Ural A. Prediction of Colle's fracture load in human radius using cohesive finite element modelling. *J Biomech* 2009; 42(1): 22–28.
22. Varga P, Baumbach S, Pahr D, et al. Validation of an anatomy specific finite element model of Colle's fracture. *J Biomech* 2009; 42(11): 1726–1731.
23. Vilayphiou N, Boutroy S, Sornay-Rendu E, et al. Finite element analysis performed on radius and tibia HR-pQCT images and fragility fractures at all sites in postmenopausal women. *Bone* 2010; 46(4): 1030–1037.
24. Keller TS. Predicting the compressive mechanical behavior of bone. *J Biomech* 1994; 27(9): 1159–1168.
25. Keyak JH, Rossi SA, Jones KA, et al. Prediction of femoral fracture load using automated finite element modelling. *J Biomech* 1998; 31(2): 125–133.
26. Cristofolini L and Viceconti M. Mechanical validation of whole bone composite tibia models. *J Biomech* 2000; 33(3): 279–288.
27. Kutzner I, Heinlein B, Graichen F, et al. Loading of the knee joint during activities of daily living measured in vivo in five subjects. *J Biomech* 2010; 43(11): 2164–2173.
28. Wong C, Mikkelsen P, Hansen L, et al. Finite element analysis of tibial fractures. *Dan Med Bull* 2010; 57(5): A4148.
29. Gray HA, Taddei F, Zavatsky AB, et al. Experimental validation of a finite element model of a human cadaveric tibia. *J Biomech Eng* 2008; 130(3): 031016.
30. Iwaki H, Pinskerova V and Freeman MAR. Tibiofemoral movement 1: the shapes and relative movements of the femur and tibia in the unloaded cadaver knee. *J Bone Joint Surg Br* 2000; 82(8): 1189–1195.
31. Nalla RK, Kinney JH and Ritchie RO. Mechanistic fracture criteria for the failure of human cortical bone. *Nat Mater* 2003; 2(3): 164–168.
32. Bessho M, Ohnishi I, Matsuyama J, et al. Prediction of strength and strain of the proximal femur by a CT based finite element method. *J Biomech* 2007; 40(8): 1745–1753.
33. Liu D, Manske SL, Kontulainen SA, et al. Tibial geometry is associated with failure load ex vivo: a MRI, pQCT and DXA study. *Osteoporos Int* 2007; 18(7): 991–997.